

# Comparison of different commercial FFDM units by means of physical characterization and contrast-detail analysis

Stefano Rivetti

*Policlinico di Modena, Modena, Italy*

Nico Lanconelli<sup>a)</sup> and Renato Campanini

*Department of Physics, University of Bologna, Italy*

Marco Bertolini, Gianni Borasi, and Andrea Nitrosi

*Arcispedale Santa Maria Nuova, Reggio Emilia, Italy*

Claudio Danielli

*Policlinico di Modena, Modena, Italy*

Lidia Angelini and Stefania Maggi

*Azienda Ospedaliera Umberto I, Ancona, Italy*

(Received 10 December 2005; revised 4 August 2006; accepted for publication 1 September 2006; published 19 October 2006)

The purpose of this study was to perform a complete evaluation of three pieces of clinical digital mammography equipment. Image quality was assessed by performing physical characterization and contrast-detail (CD) analysis. We considered three different FFDM systems: a computed radiography unit (Fuji "FCR 5000 MA") and two flat-panel units, the indirect conversion a-Si based GE "Senographe 2000D" and the direct conversion a-Se based IMS "Giotto Image MD." The physical characterization was estimated by measuring the MTF, NNPS, and DQE of the detectors with no antiscatter grid and over the clinical range of exposures. The CD analysis was performed using a CDMAM 3.4 phantom and custom software designed for automatic computation of the contrast-detail curves. The physical characterization of the three digital systems confirms the excellent MTF properties of the direct conversion flat-panel detector (FPD). We performed a relative standard deviation (RSD) analysis, for investigating the different components of the noise presented by the three systems. It turned out that the two FPDs show a significant additive component, whereas for the CR system the statistical noise is dominant. The multiplicative factor is a minor constituent for all the systems. The two FPDs demonstrate better DQE, with respect to the CR system, for exposures higher than 70  $\mu\text{Gy}$ . The CD analysis indicated that the three systems are not statistically different for detail objects with a diameter greater than 0.3 mm. However, the IMS system showed a statistically significant different response for details smaller than 0.3 mm. In this case, the poor response of the a-Se detector could be attributed to its high-frequency noise characteristics, since its MTF, NEQ, and DQE are not inferior to those of the other systems. The CD results were independent of exposure level, within the investigated clinical range. We observed slight variations in the CD results, due to the changes in the visualization parameters (window/level and magnification factor). This suggests that radiologists would benefit from viewing images using varied window/level and magnification. © 2006 American Association of Physicists in Medicine. [DOI: 10.1118/1.2358195]

Key words: digital mammography, image quality, DQE, contrast-detail

## I. INTRODUCTION

X-ray mammography places severe demands on an imaging system, such as high spatial and contrast resolution. In recent years, major improvements have occurred in the development of full-field digital detectors dedicated to mammography (FFDM). Three classes of mammography detectors were evaluated: computed radiography (CR) systems,<sup>1</sup> based on photostimulated luminescence, and indirect and direct flat-panel detectors (FPDs). CR detectors use a conventional acquisition unit to deposit x-ray energy in a photostimulable phosphor screen with delayed luminescence properties. After exposure, the screen is stimulated by a scanning laser beam,

to release the deposited energy in the form of visible light captured by a light detector. In direct FPDs, x rays are directly converted into electron-hole pairs.<sup>2,3</sup> The sensitive layer is made of a photoconductive material, such as amorphous selenium. Here, x-ray photons are converted into electric charges, which are drifted by an electric field, and finally collected by the electrodes. On the contrary, in indirect FPDs,<sup>4</sup> x rays are first converted into visible light photons. Light photons are then detected by photosensitive elements.

To assess the image quality of the various systems, spatial resolution and noise properties are evaluated, using metrics such as the modulation transfer function (MTF), normalized noise power spectra (NNPS), noise equivalent quanta (NEQ),

TABLE I. The investigated imaging systems and their principal characteristics.

Manufacturer	Fuji	General Electric (GE)	Internazionale Medico Scientifica (IMS)
System	FCR 5000 MA	Senographe 2000D	Giotto Image MD
Detection type	Computed radiography	Indirect Flat-Panel	Direct Flat-Panel
Detector material	BaFBr(Eu2+)	CsI(Tl)	aSe
Imaging area (cm × cm)	18 × 24	19 × 23	17.1 × 23.9
Array size	3540 × 4740	1914 × 2294	2016 × 2816
Pixel pitch (micron)	50	100	85
Image depth (bits)	10	14	13

and detective quantum efficiency (DQE). Image quality of different systems may be characterized using these objective measures, however medical diagnosis also involves the perception by the observer.<sup>5</sup> Images are a means for visually representing the clinical information captured by the FFDM units. Consequently, it is expected that image quality should be based on the judgment of a human observer. Contrast-detail (CD) phantoms are often used for evaluating the image performance of a system, by involving human observers. These phantoms consist in a number of objects with different size and thickness. They are used for individuating the boundary between visible and invisible objects acquired by the detectors. CD analysis is a step towards the examination of details resembling clinical lesions, even if we are aware that results obtained with CD studies could not be directly extended to clinical detection tasks. High inter- and intra-observer variability can affect the effectiveness of the subjective observations obtained with CD analyses.<sup>6</sup> The location of the gold disk in the CDMAM phantom is randomly varied among four positions. As a consequence, we utilized a four-alternative forced choice experimental paradigm (4-AFC). That helped to remove the subjectivity of the observer threshold and allowed the measurement of the object detectability on a statistical basis.

Parameters such as the NEQ and DQE have the potential for providing objective assessments of imaging performance for an image as viewed by an ideal observer. Measurements of this type allow objective comparisons to be made between different systems. More research is required to establish mathematical relationships between these measures of performance and the requirements for clinical examinations. Some studies have investigated the relationship between physical performance characteristics (MTF, NNPS, DQE) and psychophysical performance (such as those derived from CD analysis).<sup>7,8</sup> It has been reported that object detectability could be directly linked to the DQE,<sup>9,10</sup> although the response of the human eye, the system noise, and the variation of the DQE as a function of the exposure<sup>11</sup> need to be taken into account. Usually, the relationships between detector performance and object detectability are estimated for a specific detection task. In this paper, we do not make any assumptions about a particular detection task. Though, we would like to investigate the possible relationships between physical figures of merit, such as DQE, NEQ, NNPS, and CD performance.

Even if in some conditions the mammographic performance is limited by anatomical and not by detector noise,<sup>12</sup> there are other clinical conditions where the detector noise could be at least as important as the anatomical noise. For example, as reported by some studies,<sup>13,14</sup> for small objects, such as microcalcifications, the observer performance is limited by the system noise, whereas for large objects, like a nodule, the effect of anatomical fluctuations is more dominant than system noise. Further, the same detectors now used for FFDM systems could be utilized in the very near future for other imaging modalities, such as breast tomosynthesis, where the structured anatomical noise will be greatly reduced. It is therefore important to investigate the performance of a clinical detector, both in terms of physical characterization and psychophysical evaluation.

Our group has already been involved in the evaluation of digital detectors dedicated to radiology<sup>15,16</sup> and mammography.<sup>17,18</sup> In this paper, we present a comparison between three different FFDM systems, in terms of both image quality parameters (MTF, NNPS, DQE) and contrast-detail analysis. The evaluation of the systems was performed at the same standard acquisition conditions by following established international standards.

## II. MATERIALS AND METHODS

We considered three clinical systems whose main characteristics are summarized in Table I. The first system is a CR unit FCR 5000-MA manufactured by Fuji (Tokyo, Japan), the second one an indirect FPD Senographe 2000D, by GE Medical Systems (Milwaukee, WI, USA), and the last one a direct FPD Giotto Image-MD, by IMS (Bologna, Italy). For all the measurements, a common setup was chosen. All the measurements were done without the grid and the compression plate. The systems used in this study were available in a clinical setting. A low scatter condition is simulated with a 2 mm Al filter attached to the generator head, using a 28 kVp Mo-Mo beam (as recommended by IEC Standard 61267—Radiation condition RQA-M2).<sup>19</sup> For the added filtration, we used aluminum type 1199 (99.99% purity). For all image acquisitions, the exposure to the detector was measured using a calibrated mammographic ionization chamber (UNFORS 401, Unfors Instruments, Billdal, Sweden). The source-to-image distance is nearly 65 cm for all the systems.

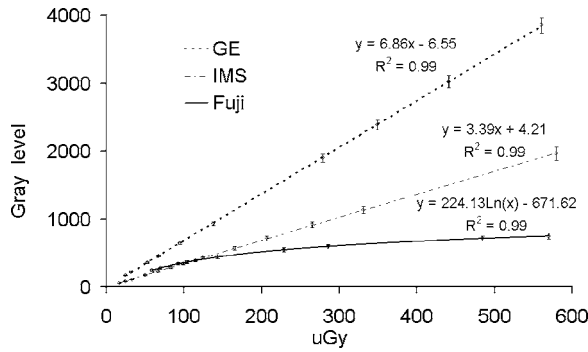


FIG. 1. Response curves for the three systems with the fitting function equation displayed (linear function for FPDs and log function for the CR system).

For the FPDs, the unprocessed images were used (only gain and bad pixel corrections were adopted), whereas for the CR system, the postprocessing has been used in FIX-MODE screen processing. In this way, one can fully control the two parameters  $S$  (sensitivity) and  $L$  (latitude). For all the images, we used  $S=139$  and  $L=2$ . The three systems were calibrated with the standard clinical procedures.

The response curve of each system was determined by exposing the detector to a wide range of uniform x-ray exposures. The average pixel values were computed from a ROI located near the chest wall section of the detector: results are depicted in Fig. 1. As expected, the two FPDs have a very linear response over a wide range of exposures (further beyond the typical clinical range), whereas the CR system response is logarithmic. Fits with linear and logarithmic functions are also shown, respectively, for the FPDs and the CR system. Due to the logarithmic response of the CR system, all the image data used for the physical measurements were “linearized” by means of the fitted response function.

### A. Physical characterization

The presampling MTF was measured by using the slit technique: an oversampled line spread function (LSF) was obtained using a  $10\ \mu\text{m}$  tantalum slit. The slit was oriented at a small angle (smaller than  $5^\circ$ ) with respect to the pixel array. An exponential fitting of the oversampled LSF was performed, in order to reduce the contribution of the noise in the tails. The MTF reported is the average between those obtained along the two orthogonal axes.

To characterize the system noise, both NNPS and relative standard deviation (RSD) analysis were performed. These figures were computed from flat field images at different exposure levels. Four images were obtained for each exposure level, and for each image four ROIs with fixed size of about  $25 \times 25\ \text{mm}^2$  were extracted, Fourier transformed, and averaged, to compute the 2D NPS. The NPS was then normalized for the squared mean signal value of the ROI, obtaining the NNPS. The 1D NNPS was obtained by excluding the axes and by averaging the 2D spectrum along a radial line. The product of NNPS and exposure (or air kerma) is independent of exposure for a linear, quantum-limited detector.<sup>2</sup> Thus, we

calculated this product for assessing the quantum-limited condition of the three detectors. The same ROIs used for NNPS calculation were also used to perform the RSD analysis. RSD (i.e., standard deviation divided by average signal value) was calculated inside the ROI. The average RSD squared over all the ROIs was then computer fit using the following function:

$$\text{RSD}^2 = \left( \frac{\sigma_{\text{TOT}}}{x} \right)^2 = \frac{\alpha}{x} + \beta + \frac{\gamma}{x^2} \quad (1)$$

where  $x$  is the x-ray exposure, and the three parameters  $\alpha$ ,  $\beta$ , and  $\gamma$  represent the contributions of the quantum-statistical (Poisson) noise source of a dose related (multiplicative) noise source and of a dose independent (additive) noise source, respectively.<sup>15,20</sup> Equation (1) derives from the definition of the total variance  $\sigma_{\text{TOT}}^2$ . In fact, for an image  $\sigma_{\text{TOT}}^2$  can be described as the sum of three terms related to Poisson, multiplicative, and additive noise. The three components result to be proportional to exposure (Poisson noise) and to the square of exposure (multiplicative noise) and are exposure independent (additive noise):

$$\sigma_{\text{TOT}}^2 = \sigma_{\text{POIS}}^2 + \sigma_{\text{MULT}}^2 + \sigma_{\text{ADD}}^2 = \alpha x + \beta x^2 + \gamma. \quad (2)$$

For a digital detector, the additive factor can be interpreted as the noise connected to electronics, whereas the multiplicative component could be related to a fixed pattern noise not removed by flat-field correction. In order to verify the validity of Eqs. (1) and (2), we performed the RSD analysis both on single images and on difference images.<sup>20</sup> Single images are the same flat-field images used for NNPS calculation, whereas difference images are obtained as the difference of two single images acquired at the same exposure. The difference images should not contain the multiplicative noise caused by fixed patterns. NEQ was then computed by the following formula:<sup>21</sup>

$$\text{NEQ}(f) = \frac{\text{MTF}^2(f)}{\text{NNPS}(f)}. \quad (3)$$

Half-value layer (HVL) measurements were made with the 2 mm aluminum foil filtered beam. HVL was estimated from logarithmic interpolation of the measured exposure values. We estimated the photon fluence as described by Boone.<sup>22</sup> In particular, we calculated the x-ray spectrum by means of a spectral model developed for mammography,<sup>23</sup> and using mass energy-absorption coefficient data available from the National Institute of Standards and Technology (NIST) database. DQE was finally calculated as

$$\text{DQE}(f) = \frac{\text{NEQ}(f)}{q}, \quad (4)$$

where  $q$  is the number of photons per unit area.

### B. Contrast-detail analysis

We achieved the contrast-detail investigation by using the CDMAM 3.4 phantom developed in Nijmegen (Artinis Medical Systems B.V., Arnhem, The Netherlands). In order

to compare physical and psychophysical image quality parameters we adopted a configuration as similar as possible to that used for physical parameters' evaluation. Hence, the acquisition parameters were the same used for the DQE calculation (28 kV Mo-Mo with a beam filtered with 2 mm aluminium foil). The CDMAM phantom consists of a matrix of squares (16 rows and 16 columns), each one containing two identical gold disks. The first disk is located in the center of the square, whereas the second disk is placed in a randomly chosen corner. For verifying the detection of each disk, the observer has to indicate the corner where the eccentric disk is located. The range of object sizes and thicknesses of the phantom covers the typical values of clinical microcalcifications and small masses. The gold disks ranged in diameter between 60  $\mu\text{m}$  and 2 mm. Their thicknesses vary between 0.03 and 2 microns of gold, resulting in a radiation contrast range of about 0.5%–30% at standard mammography exposure conditions. Disks belonging to the same row have constant thickness and a logarithmically varying diameter. The phantom was placed as close as possible to the chest wall edge of the detector, with the smaller details near to the chest wall side. It was randomly repositioned after each exposure, in order to get images with various phantom-object positions with respect to the pixels of the detector and to avoid that a small detail always remains in the same detector area. In fact, given that digital systems are not shift invariant, especially for small details, the perceived contrast of an object depends on its alignment with respect to the sampling grid.<sup>24</sup>

Images were evaluated on two dedicated high-resolution monitors (Barco MGD521, 2048  $\times$  2560 matrix, 8 bit, max luminance: 600  $\text{cd}/\text{m}^2$ ). The operating conditions, such as ambient light, visualization parameters, and the software used for CD evaluation, were chosen to maximize the reading performance of the observers. The images were presented on the monitor, with the room light off, using suitable magnification factor, brightness, and contrast. The contrast and the brightness (window/level) were fixed at the same value for the three systems. We tested different visualization conditions (two window/levels and two magnification factors). We developed apposite software, for facilitating the CDMAM reading by human observers.<sup>25</sup> The software is written in IDL<sup>TM</sup> language (RSI, Pearl East Circle Boulder, CO), and incorporates all the features of the CDMAM phantom (sizes, thicknesses, and positions of all the details). Observers can select which square within the phantom they want to visualize and choose the location (vertex of the square) where the eccentric gold disk is supposed to be. Crops are randomly rotated by an angle of 90°, 180°, or 270° to prevent any “memory effects” in the readers about the location of the disks within each square. When several phantom images are acquired in the same acquisition conditions, the software visualize in a random order the corresponding squares coming from the different realizations. Observers had no restrictions on viewing time for each reading session. Five experienced operators evaluated the entire image set (12 conditions: three systems for two exposures, plus an additional magnification factor and an additional window/level for each system); six images per setting were assessed by the

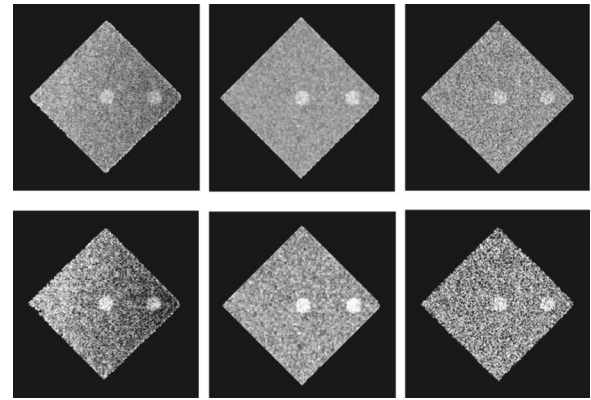


FIG. 2. Examples of a CDMAM detail as displayed by the three systems at the two different window-levels used. (Left: Fuji images; center: GE images; right: IMS images.) (Top row: window/level 1; bottom row: window/level 2.)

observers. Each observer independently reviewed the images of one setting in one session; the various settings were presented in a random fashion to reduce systematic errors. All five observers read all of the phantom images in all used experimental conditions. During scoring sessions all readers were sitting at the same distance from the monitor. Observers could not change the magnification factor or the window/level. The three systems were analyzed at two different exposures (70 and 140  $\mu\text{Gy}$ ), two different magnification factors (about 2 $\times$  and 5 $\times$ ), and two different fixed window/levels. The two exposures were chosen among those considered for the physical evaluation of the system and correspond roughly to two extreme clinical values of the exposure reaching the detector under the breast. The two magnification factors were chosen to approximately represent the magnification that occurs when viewing a single mammogram on a dedicated 5 megapixel display and when a digital lens is used in visualization software, respectively. The two window/levels (named in the following W/L 1 and W/L 2) differ in the visualization contrast, i.e., W/L 2 has the same brightness, but an increased contrast, with respect to W/L 1, as shown in Fig. 2. In particular, for W/L 1 the contrast of the original image is amplified by a factor equal to 15, while for W/L 2 the amplification is 30. Thus, W/L 2 tends to have greater enhancement of the system noise. The brightness value was chosen in such a way that the background level of the phantom corresponded to a luminance of about 50  $\text{cd}/\text{m}^2$ . The first window/level (W/L 1) was selected as an average of the best visualization conditions chosen by the observers on a preliminary study. Before starting the reading task, they visualized some CDMAM images and they were free to change the visualization parameters, in order to get the best visibility of the details.

Several parameters can be extracted from a CD analysis.<sup>26</sup> We decided to compute, for each investigated setting, a CD curve, together with two different figures: correct observation ratio (COR) and image quality figure (IQF), defined as follows:

$$\text{COR} = \frac{\text{Correct observations}}{\text{Total number of squares}} \cdot 100\%, \quad (5)$$

$$\text{IQF} = \sum_{i=1}^{16} C_i \cdot D_{i,\min}, \quad (6)$$

where  $C_i$  is the contrast (gold thickness) of column  $i$  and  $D_{i,\min}$  denotes the threshold diameter in contrast column  $i$ . Summation over all contrast columns yields the IQF. The CD curves were obtained by averaging together the data from each single observer. Each CD curve is plotted with error bars corresponding to  $\pm 1$  standard deviation from the mean. CD curves are compared with theoretical data estimated from the Rose model.<sup>27</sup> According to this model, the contrast threshold  $C_{TR}$  for a circular object of diameter  $\alpha$  can be estimated as

$$C_{TR} = \frac{2k}{\alpha \sqrt{\pi q \text{DQE}(0)}}, \quad (7)$$

where  $\text{DQE}(0)$  is the DQE at zero spatial frequency and  $k$  represents the minimum SNR threshold needed by the observer for detecting the object. To test the statistical significance of the difference between two different CD curves, a nonparametric test (Mann-Whitney) was performed.<sup>28</sup> The test was first done by including all phantom details together, and then by grouping them into two subsets: large and medium details ( $>0.3$  mm) and small details ( $\leq 0.3$  mm). The statistical tests were performed with the SPSS package (version 13.0; SPSS Inc., Chicago, IL, USA). A  $p$ -value of less than 0.05 was considered to indicate a statistically significant difference.

### III. RESULTS AND DISCUSSION

#### A. Physical characterization

##### 1. Modulation transfer function

Figure 3 shows the presampling MTF curves of the three FFDM devices. The MTF of the FPDs is practically identical along the two axes, whereas the CR system has different MTF characteristics along the scanning and subscanning directions. Actually, very small differences (less than 2%) were observed between gate and data line directions for the two FPDs. In Fig. 4 the MTF curves relative to the two orthogo-

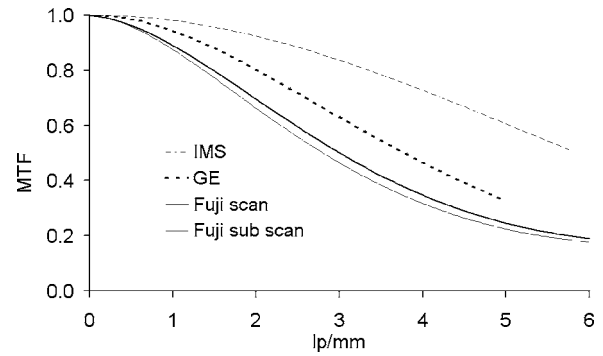


FIG. 3. Presampling MTF curves for the three systems. For the two FPDs, the differences between the MTF in the two directions are very small (within 2%). Thus, only the MTF along one direction is plotted. The direct conversion system shows an excellent MTF, as expected.

nal directions are illustrated. The MTF of the three systems did not show any dependency from the exposure, at least in the range of the investigated exposures. As expected, the direct conversion detector demonstrates better spatial resolution than the other systems. Indeed, the a-Se-based IMS unit has a MTF equal to about 50% at its Nyquist frequency of 5.88 lp/mm.

#### 2. Noise analysis

In Fig. 4 results of the RSD analysis estimated on single images are depicted: RSD is plotted as a function of the air kerma. The experimental data are fitted with the function given in Eq. (1); the coefficients of the fitting functions are summarized in Table II. These parameters correspond to the different component of the noise. It is worth noting that the two FPDs show a significant additive component (especially the IMS system), whereas for the CR system the statistical noise is dominant. The multiplicative factor is a minor constituent for all the systems. As a general tendency, the Fuji total noise tends to increase less rapidly, as the exposure decreases, with respect to the other systems' noise. This suggests that better system response exists at low exposures, relative to the FPDs. However, all the three systems seem to be quantum noise limited at clinical exposures, since the additive component of the FPDs gives a significant contribution only at very low exposures, as illustrated in the following. The Poisson and additive components estimated on

TABLE II. Values of the main noise components for the three systems, as estimated by RSD analysis. For each estimated component, the top row shows fitted values estimated on single images, whereas the bottom row shows fitted values on difference images.

Components	Coefficient	Fuji	GE	IMS
Poisson	$\alpha$	$(58 \pm 7) \times 10^{-3}$	$(23 \pm 3) \times 10^{-3}$	$(40 \pm 3) \cdot 10^{-3}$
		$(52 \pm 7) \times 10^{-3}$	$(26 \pm 3) \times 10^{-3}$	$(36 \pm 3) \times 10^{-3}$
Multiplicative	$\beta$	$(3 \pm 0.7) \times 10^{-5}$	$(0.1 \pm 0.08) \times 10^{-5}$	$(2 \pm 0.8) \times 10^{-5}$
		$(0.8 \pm 0.2) \times 10^{-5}$	$(0.04 \pm 0.01) \times 10^{-5}$	$(0.6 \pm 0.2) \times 10^{-5}$
Additive	$\gamma$	$(1.4 \pm 0.2) \times 10^{-3}$	$(150 \pm 40) \times 10^{-3}$	$(920 \pm 50) \times 10^{-3}$
		$(1.3 \pm 0.2) \times 10^{-3}$	$(120 \pm 40) \times 10^{-3}$	$(950 \pm 50) \times 10^{-3}$

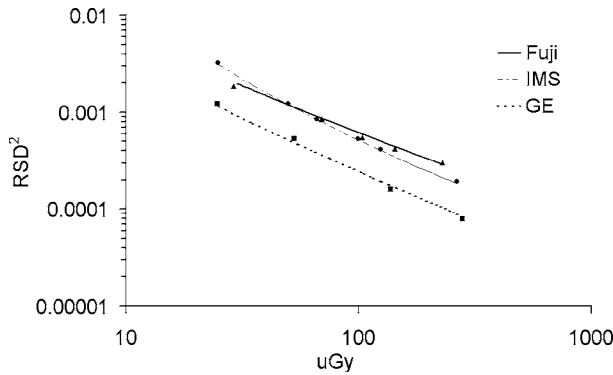


FIG. 4. RSD analysis: experimental data for RSD<sup>2</sup> values (points on the graph) and the fitting curves used for estimating the various components of the systems' noise. The Fuji total noise tends to increase less rapidly, as the exposure decreases, with respect to the other systems' noise. Plotted values correspond to RSD estimated on single images.

difference images are in good agreement with the parameters fitted on single images, indicating that Eqs. (1) and (2) provide a good model for describing the different noise components.

An example of the 2D NNPS is illustrated in Fig. 5 for the 70  $\mu$ Gy exposure level. For better visualization of the entire spectra, the central points have been zeroed. The direct conversion system has a nearly flat noise, and its value is higher than that of the other systems, as the brighter spectra shows. The noise of the other two systems decreases with increasing frequency, as expected by a phosphor-based detector. The NNPS of the CR system drops rapidly with increasing frequency. The 1D NNPS basically confirms this trend, as shown in Fig. 6 for the three systems at several exposures. Here it is possible to see that the a-Se-based detector produces a higher noise, especially at high frequencies. Figure 7 illustrates the product of NNPS multiplied by the exposure (air kerma), as a function of the spatial frequency. As already noted, for a strictly quantum noise limited detector, this product should remain constant for every exposure. The CR system, due to its low additive noise, confirms a nearly ideal behavior and seems to be quantum noise limited for the entire range of investigated exposures. On the other hand, results for the two FPDs show a noticeable exposure dependency. The two lowest exposures (up to about 50  $\mu$ Gy) are distinct from the others, showing that for these exposure val-

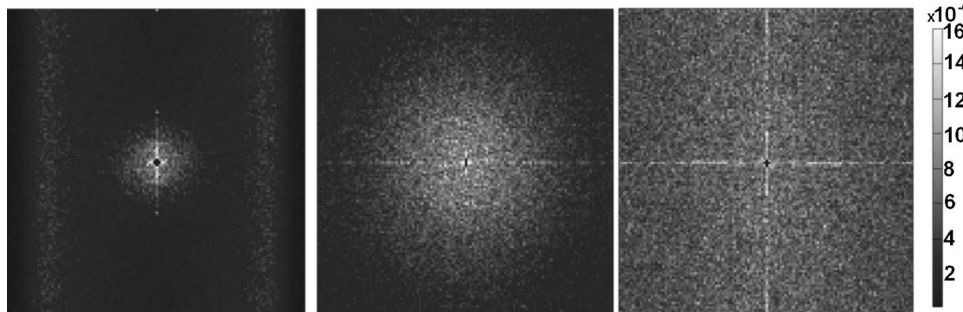


FIG. 5. Example of 2D NNPS image for the three systems. (Left: Fuji image; center: GE image; right: IMS image.) For better visualization of the entire spectra, central points are zeroed. The gray-level bar on the right refers to all three spectra and connects NNPS values in  $\text{mm}^2$  to the gray level of the images.

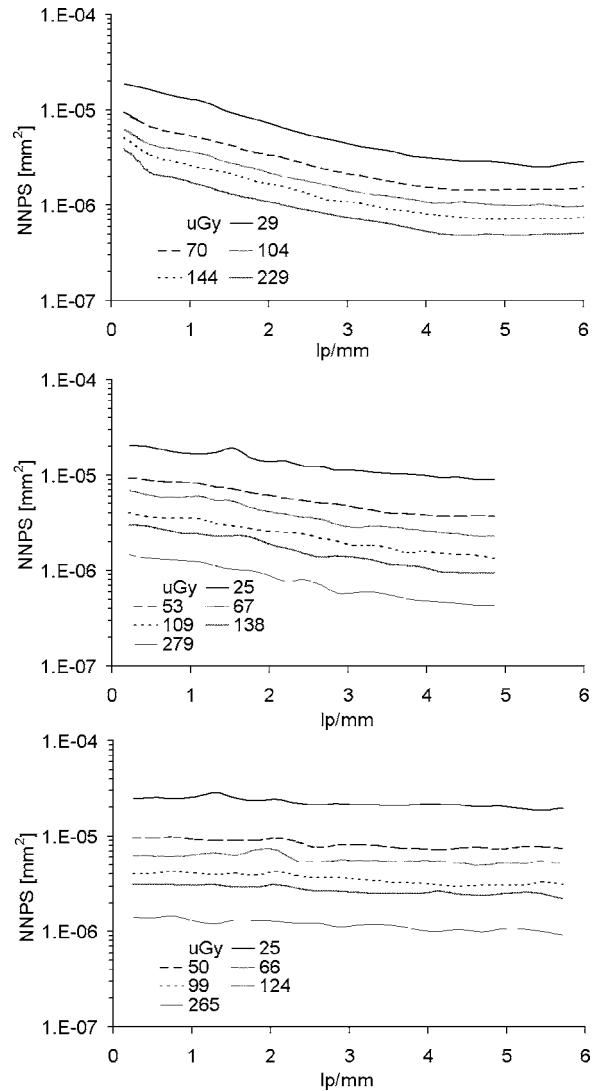


FIG. 6. 1D NNPS for the three systems at various exposures. (Top: Fuji; center: GE, bottom: IMS.) 1D NNPS is obtained on the radial direction from the 2D NNPS.

ues the two systems seem not to be limited by quantum noise. This is likely due to the significant additive component noise, as highlighted by the RSD analysis.

### 3. Quantum efficiency

Figure 8 shows the NEQ as a function of the spatial frequency for the three systems and the investigated exposures.

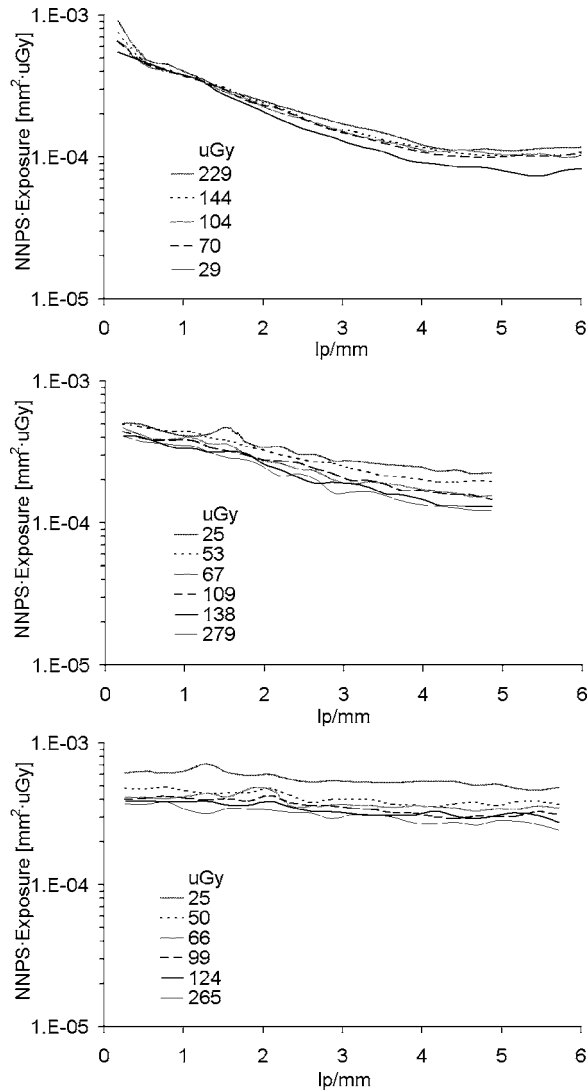


FIG. 7. NNPS multiplied by air kerma for the three systems. (Top: Fuji; center: GE, bottom: IMS.) This product should be independent from the exposure, for a strictly quantum noise limited detector.

As expected, the NEQ increases with exposures for all the systems, even if for the CR system the rising is less accentuated than that of the FPDs. As a consequence, the CR system has a higher NEQ than the FPDs for low exposures, whereas the FPDs outperform the CR system at high exposures. The NEQ of the three systems seems to become comparable at an exposure level of about  $70 \mu\text{Gy}$ .

The measured HVL for the Fuji, GE, and IMS systems were 0.59, 0.61, and 0.61 mm Al, respectively. The fluence parameter  $q$  needed for the DQE computation was estimated to be 44 400, 45 800, and 45 800 photons/ $\text{mm}^2/\text{mR}$ , respectively, for the three systems.

Figure 9 illustrates the DQE of the three FFDM systems at the various exposures. We note that the DQE of the two FPDs is noticeably lower at small exposures, as the electronic noise becomes more significant and the detectors tend to deviate from the quantum noise limited condition. On the other hand, the CR system has a completely different behavior, since its DQE reaches the maximum at low exposures.

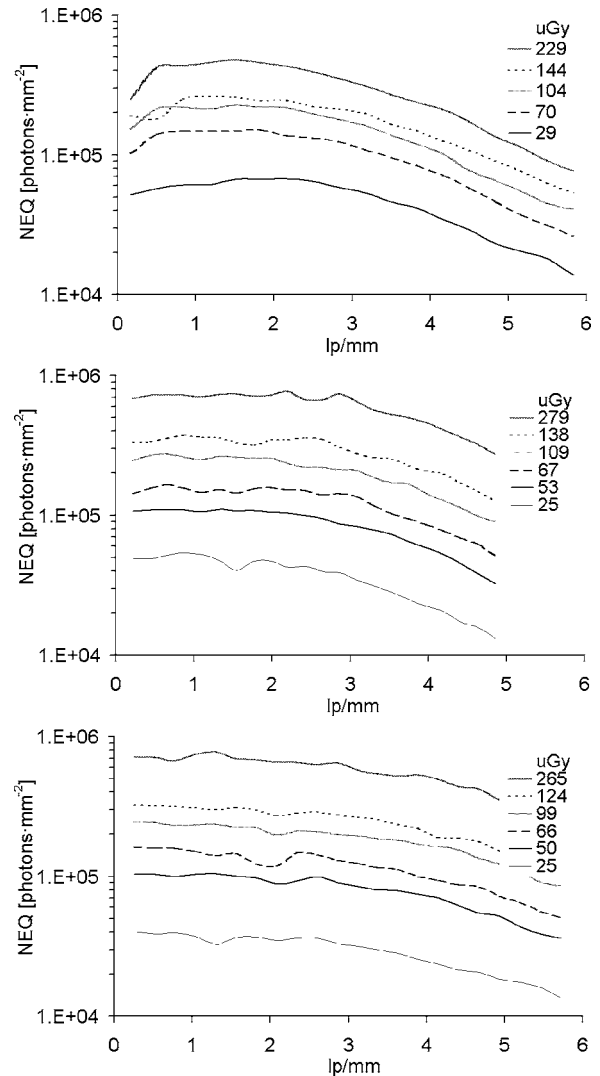


FIG. 8. NEQ for the three systems at various exposures. (Top: Fuji; center: GE, bottom: IMS.) The NEQ of the three systems is fairly comparable at an exposure of about  $70 \mu\text{Gy}$ .

The two FPDs have a higher DQE than the CR unit over a large range of investigated exposures. As with the NEQ, the DQE curves of the three systems are comparable at an exposure level of about  $70 \mu\text{Gy}$ , lower than the typical clinical exposure of  $100\text{--}130 \mu\text{Gy}$ . It is worth remarking that the DQE of the two FPDs has a considerable drop at low exposures (especially the lowest two), whereas the CR system shows a DQE that is nearly independent from the exposure. Once again, this confirms that the two FPDs seem to be dominated by electronic noise at exposures smaller than about  $50 \mu\text{Gy}$ .

Figure 10 illustrates as the DQE of the three systems varies with exposure, at a spatial frequency of  $1.5 \text{ lp/mm}$ . It is possible to point out the different behaviors of the CR and the FPD systems. The former present a maximum DQE for low exposures, whereas the FPDs have a DQE that increases with exposures. This diagram shows that the Fuji system, due to its low additive noise, has a DQE practically independent from the air kerma. The DQE of the two FPDs begins to

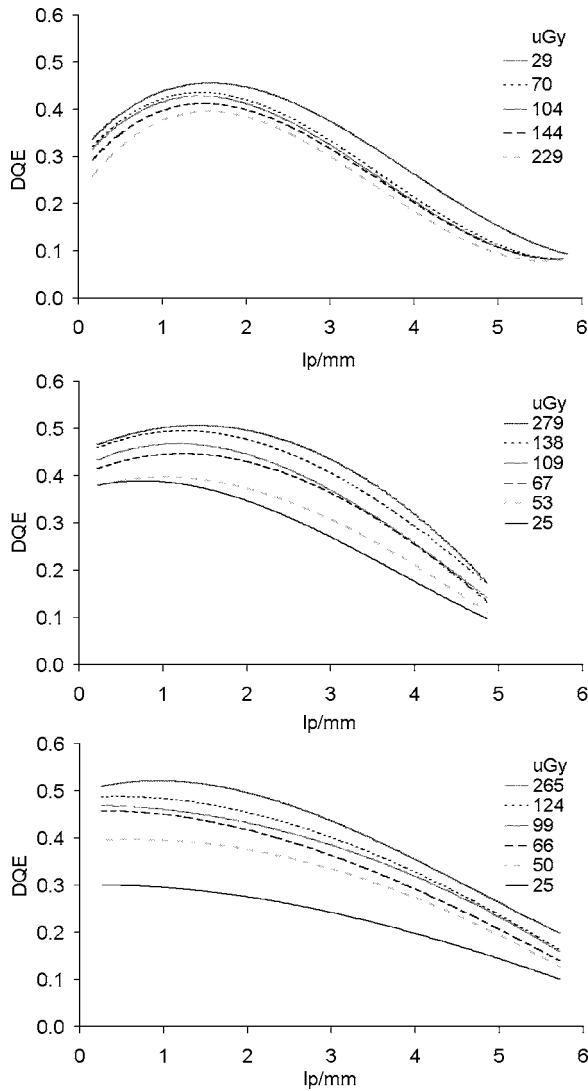


FIG. 9. DQE for the three systems at various exposures. (Top: Fuji; center: GE, bottom: IMS.) DQE curves are obtained by a fourth grade polynomial fitting of the experimental data. The DQE curves of the three systems are comparable at an exposure level of about 70  $\mu\text{Gy}$ .

be approximately constant over the exposure at an air kerma level of about 70–90  $\mu\text{Gy}$ . Thus, the two FPDs analyzed seem to work in a quantum noise limited condition for exposures greater than about 80  $\mu\text{Gy}$ .

The IMS Giotto Image-MD unit analyzed shows a worse DQE with respect to systems that utilized the same (or a similar) detector,<sup>29–31</sup> even if the MTF is comparable, though the IMS system presents a higher noise, probably derived by a nonperfect flat-field correction or by a poorly calibrated detector. Results for the Fuji and the GE units are comparable to others obtained on the same systems.<sup>1,4,32</sup>

**B. Contrast-detail analysis**

**1. System comparison**

Figure 11 shows the CD curves for the three FFDM systems at the two analyzed exposures (70 and 140  $\mu\text{Gy}$ ). We displayed the images with magnification equal to about 5×

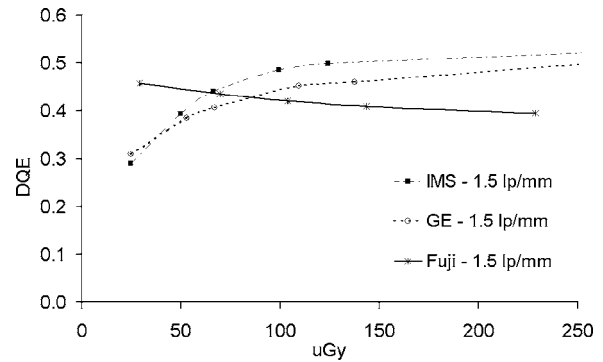


FIG. 10. Comparison of the DQE versus incident exposure (air kerma) for a spatial frequency of 1.5 lp/mm. The Fuji DQE is fairly independent from exposures, whereas FPDs show a DQE that increases as the exposure increases. This behavior is repeated also at other spatial frequencies.

and window/level W/L 1. For details with a diameter greater than 0.3 mm, the response of the three systems is not statistically different at either exposure. On the other hand, the IMS systems have a statistically significant different response for detail smaller than 0.3 mm: for the higher exposure, IMS versus GE differ with  $p < 0.05$ , while for the lower exposure IMS versus GE differ with  $p < 0.02$ , and IMS versus Fuji differ with  $p < 0.03$ .

**2. CD response in different conditions**

Figure 12 shows a comparison of the CD response of the three systems between the two investigated exposures. Even

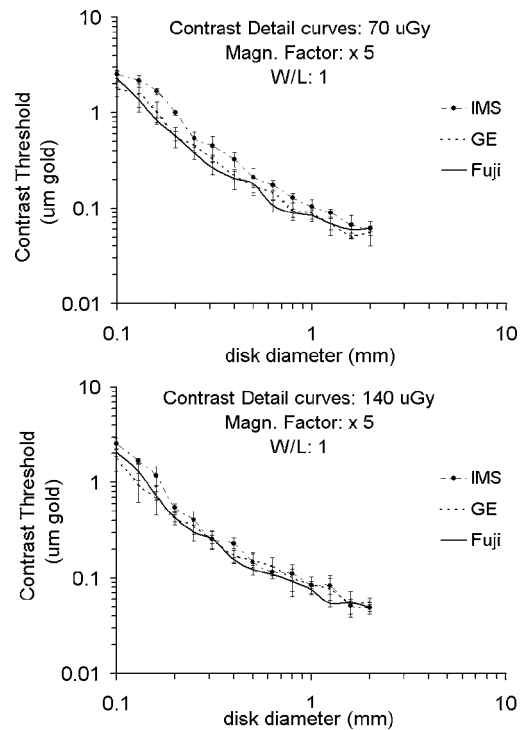


FIG. 11. CD curves for the three systems at the two analyzed exposures. (Top: 70  $\mu\text{Gy}$ ; bottom: 140  $\mu\text{Gy}$ .) The error bars correspond to  $\pm 1$  standard error from the mean. These curves are obtained with the optimal window/level (W/L 1) and with the bigger magnification factor used ( $\times 5$ ).

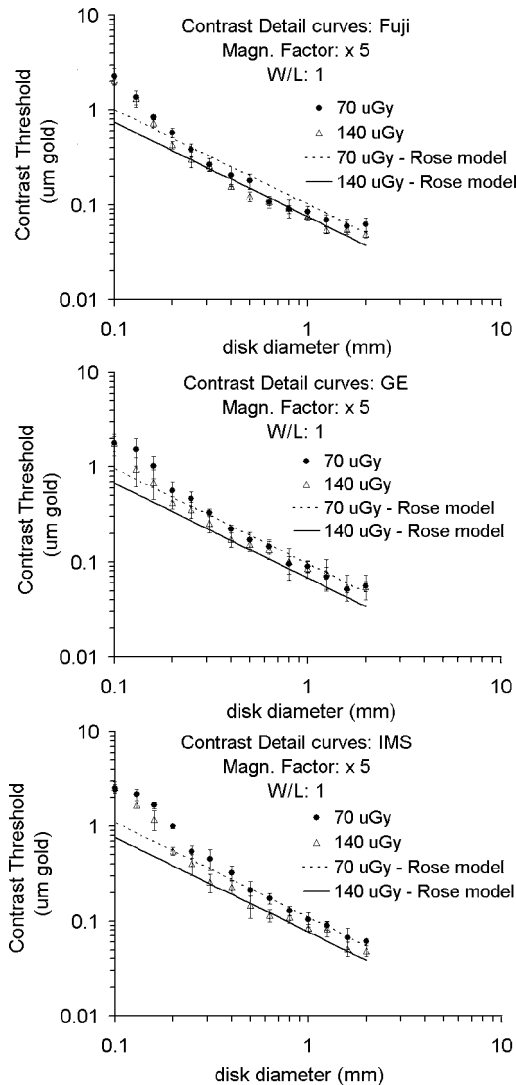


FIG. 12. Comparison of the CD experimental data for the three system at the two investigated exposures. (Top: Fuji; center: GE; bottom: IMS.) The error bars correspond to  $\pm 1$  standard error from the mean. These curves are obtained with the optimal window/level (W/L 1) and with the bigger magnification factor used ( $\times 5$ ). Theoretical curves estimated from the Rose model described by Eq. (7) are also shown with solid and dotted lines.

if in general the visibility is slightly better for the higher exposure, as expected, this difference is almost always non-significant. Only the IMS system gives a statistically different response ( $p < 0.05$ ) for small details. This confirms the fact that the analyzed a-Se detector, as already seen, gives a worse result for small details, especially at low exposures. Generally speaking, the visibility of the details is not dependent from the exposure, within the investigated clinical range. Theoretical curves calculated from Eq. (7) are also shown in the plots. As reported elsewhere,<sup>27</sup> this model agrees well with experimental data, except for small details, where a more complete model including the human visual response and the system noise should be adopted. Theoretical curves have been obtained by using a threshold  $k$  equal to 4.5, 5, and 6, respectively, for Fuji, GE, and IMS systems.

Figure 13 illustrates CD curves for the three FFDM sys-

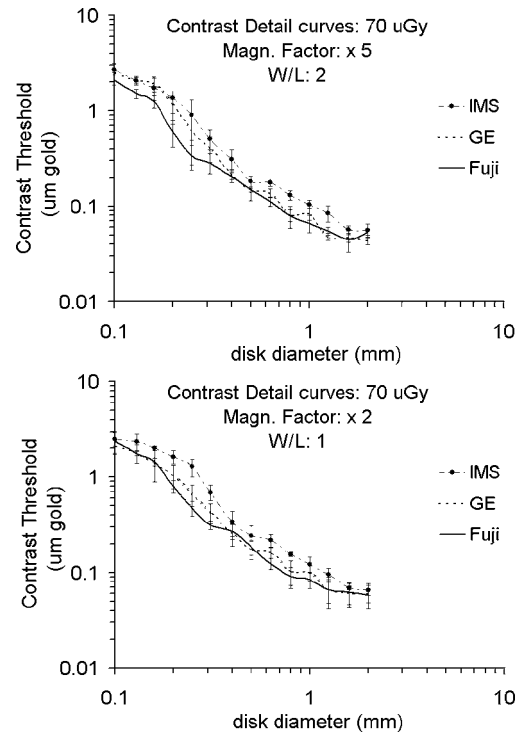


FIG. 13. CD curves for the three systems at air kerma equal to  $70 \mu\text{Gy}$ , for two different magnification-window/level conditions. (Top: Magnification factor 5 – window/level N.2; bottom: Magnification factor 2 – window/level N.1.) The error bars correspond to  $\pm 1$  standard error from the mean.

tems at two other viewing conditions: a second window/level (W/L 2 with same magnification level  $5\times$  as before) and a second magnification factor ( $2\times$  with the initial window/level W/L 1). In both cases the air kerma is equal to  $70 \mu\text{Gy}$ . In the first case (i.e., initial magnification factor and different window/level W/L 2), IMS versus Fuji curves are statistically different for the entire range of details size ( $p < 0.05$ ), and IMS versus GE curves are statistically different for details greater than  $0.3 \text{ mm}$  ( $p < 0.03$ ). In addition, GE versus Fuji curves are statistically different for details smaller than  $0.3 \text{ mm}$  ( $p < 0.02$ ). Thus, with respect to the initial visualization parameters, the window/level with higher contrast tends to penalize the FPDs, with respect to the CR system. The worse performance of the FPDs at high contrasts could be related to the fact that their high-frequency noise is higher than the CR noise. In fact, this noise seems to be further enhanced by the higher contrast of the images when using W/L 2. In the second case (i.e., initial window/level, and different magnification factor  $2\times$ ), IMS versus Fuji curves are statistically different for the entire range of details size ( $p < 0.05$ ), and IMS versus GE curves are statistically different for details smaller than  $0.3 \text{ mm}$  ( $p < 0.02$ ). The results with this smaller magnification factor basically reflect their initial results; the main difference is that now IMS gives worse CD results than Fuji for the entire range of detail sizes.

Finally, we made a comparison of the CD response of the three systems by analyzing the differences between the two window/levels and the two magnification factors. The only statistically significant differences are for details smaller than

TABLE III. Values of correct observation ratio (COR) and image quality figure (IQF) for all the investigated contrast-detail conditions.

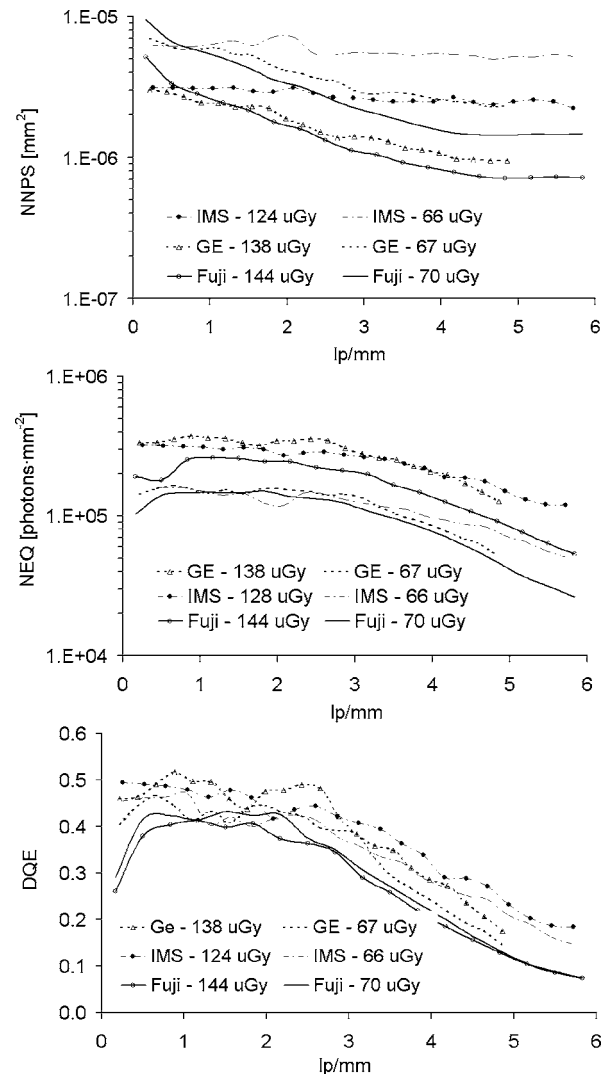
		140 $\mu$ Gy	70 $\mu$ Gy	70 $\mu$ Gy	70 $\mu$ Gy
		W/L 1	W/L 1	W/L 2	W/L 1
		Magn. $\times 5$	Magn. $\times 5$	Magn. $\times 5$	Magn. $\times 2$
Fuji	COR (%)	50 $\pm$ 2	46 $\pm$ 3	48 $\pm$ 4	43 $\pm$ 3
	IQF (mm $\cdot\mu$ m)	22 $\pm$ 1	25 $\pm$ 3	25 $\pm$ 3	29 $\pm$ 3
GE	COR(%)	48 $\pm$ 5	44 $\pm$ 3	44 $\pm$ 3	40 $\pm$ 4
	IQF (mm $\cdot\mu$ m)	23 $\pm$ 4	26 $\pm$ 3	31 $\pm$ 5	32 $\pm$ 5
IMS	COR (%)	45 $\pm$ 3	37 $\pm$ 3	36 $\pm$ 3	32 $\pm$ 4
	IQF (mm $\cdot\mu$ m)	27 $\pm$ 2	35 $\pm$ 3	37 $\pm$ 5	44 $\pm$ 5

0.3 mm visualized with the GE system in both cases ( $p < 0.01$  for the two W/L curves and  $p < 0.05$  for the two magnification factor curves). Nevertheless, slight variations are present in most cases. This suggests that radiologists should not use a fixed set of visualization parameters, but they should try different window/levels and different magnification factors, in order to visualize the different type of structures in an optimal way. From our data, the Fuji and the IMS systems seem to be more stable, with respect to the visualization parameters (window/level and magnification factor).

Table III summarizes the results of all the investigated conditions in terms of COR and IQF. Results are consistent with those derived from the CD curves, even if in this case one cannot discriminate between small and large details. Some tendencies pointed out with the comments of the CD curves are here accentuated. First of all, for the lower exposure the IMS system seems to give a clearly worse result than the others. There is also a noteworthy difference for the a-Se panel between the two exposures. Even if COR and IQF can condense the behavior of a system in a single figure, we believe that the CD curves are a more complete and comprehensible way to assess the visibility performance of a unit. CD results are not dissimilar to those obtained in analogous conditions on the same systems<sup>13,33</sup> or on systems with the same detector.<sup>29</sup>

### 3. Connections between physical and psychophysical evaluation

In order to explore how the CD analysis could be related to the physical evaluation, we reported NNPS, NEQ, and DQE of the three systems at the two exposures used for the CDMAM acquisitions (Fig. 14). It is worth remarking that neither the NEQ nor the DQE seems to be correlated with the CD response, since, for example, the Fuji system gives comparable or inferior NEQ and DQE results, but the CD curve is not worse than the others at all. Besides, the IMS system presents comparable or better NEQ and DQE, but lower visibility for small details. From our data, it seems that the NNPS can be a more important feature, for a better comprehension of the CD data. Indeed, the IMS unit provides a higher noise, especially at higher frequency, at both exposures. This noise seems not to be dangerous for large details, since their visibility is fairly comparable with that obtained

FIG. 14. Comparison of NNPS (top), NEQ (center), and DQE (bottom) for the three systems at air kerma equal to 70 and 140  $\mu$ Gy.

with the other systems. However, we believe that this high-frequency noise could impair the visibility of small details, in spite of the excellent MTF of the a-Se panel. This seems to be in agreement with other studies,<sup>13,14</sup> which show that a high system noise could be detrimental for the visibility of small objects. The phase dependence of the small details could also make their detection more difficult, especially for systems with high MTFs. However, we reduced this effect by moving the phantom after each exposure. According to Moy,<sup>34</sup> when the MTF of a digital system extends further beyond the Nyquist frequency, the aliasing so introduced enhances the noise and can reduce the benefit of the excellent MTF feature. In this case, we see this effect in the IMS detector, which shows a very high MTF, but at the same time a considerable high-frequency noise.

It is worth noting that, despite the smaller pixel size, the CR system and the a-Se panel are not better for small details. Furthermore, the better noise quality of the indirect conversion FPD and of the CR system seems to give a slightly better visibility of the smallest details, especially at the lower

exposure condition investigated. From these results, it seems that the pixel size is not a good indicator of small details detection performance. It is clearly important to have a detector with good noise properties. We would like to remark that the conclusions we obtained are valid for the three analyzed systems in a clinical environment. Further work has to be done in order to assess if these results could be extended also to other FFDM systems.

#### IV. CONCLUSION

The physical characterization of the three digital systems confirms the excellent MTF properties of the direct conversion FPD. On the other hand, the FPDs showed a higher additive noise component (especially the IMS system), which is responsible for a deviation from the quantum noise limited condition for the lower exposures (lower than about 80  $\mu\text{Gy}$ ). However, the two FPDs give a better DQE, with respect to the CR system, for exposures higher than 70  $\mu\text{Gy}$ .

The CD analysis pointed out that the visibility of the three systems is not statistically different at both exposures for details with a diameter greater than 0.3 mm. On the other hand, the IMS system has a statistically significant different response for details smaller than 0.3 mm. The worse response of the analyzed a-Se detector could be related to its high-frequency noise, since its MTF, NEQ, and DQE are not inferior to those of the other systems. From the CD results, it appears that pixel size alone is not a significant parameter for having a good detection of small objects, since noise features are essential as well. Thus, it is important to have an appropriate pixel size, which allows good noise performance, in order to detect small details. The visibility of the details is not dependent on the exposure within the investigated clinical range (only the IMS system gives a statistically different response for small details at the lowest exposure). Finally, the Fuji and IMS systems seem to be more stable, with respect to the visualization parameters (window/level and magnification factor), since the response is not statistically different for the investigated conditions.

#### ACKNOWLEDGMENT

The authors would like to thank Professor John M. Boone for his interest in the present work and for his helpful suggestions.

<sup>a)</sup> Author to whom correspondence should be addressed: Dipartimento di Fisica, Viale Berti-Pichat 6/2, I-40127 Bologna BO, Italy. Electronic mail: nico.lanconelli@bo.infn.it. <http://www.bo.infn.it/~lanconelli/>

<sup>1</sup>J. A. Seibert, J. M. Boone, and V. N. Cooper, "Determination of imaging performance of a photostimulable phosphor system for digital mammography," *Proc. SPIE* **4682**, 447–456 (2002).

<sup>2</sup>R. S. Saunders, Jr., E. Samei, J. L. Jesneck, and J. Y. Lo, "Physical characterization of a prototype selenium-based full field digital mammography detector," *Med. Phys.* **32**(2), 588–599 (2005).

<sup>3</sup>W. Zhao, W. G. Ji, A. Debie, and J. A. Rowlands, "Imaging performance of amorphous selenium based flat-panel detectors for digital mammography: Characterization of a small area prototype detector," *Med. Phys.* **30**, 254–263 (2003).

<sup>4</sup>S. Vedantham, A. Karellas, S. Suryanarayanan, D. Albagli, S. Han, E. J. Tkaczyk, C. E. Landberg, B. Opsahl-Ong, P. R. Granfors, I. Levis, C. J. D'Orsi, and R. E. Hendrick, "Full breast digital mammography with an amorphous silicon-based flat panel detector: Physical characteristics of a

clinical prototype," *Med. Phys.* **27**(3), 558–567 (2000).

<sup>5</sup>E. A. Krupinski, "Importance of perception research in medical imaging," *Radiat. Med.* **18**, 329–334 (2000).

<sup>6</sup>G. Cohen, D. L. McDaniel, and L. K. Wagner, "Analysis of variations in contrast-detail experiments," *Med. Phys.* **11**(4), 469–473 (1984).

<sup>7</sup>H. Roehrig, E. Krupinski, and T. Yu, "Physical and psycho-physical evaluation of digital systems for mammography," *Proc. SPIE* **2436**, 124–134 (1995).

<sup>8</sup>R. Aufrichtig, "Comparison of low contrast detectability between a digital amorphous silicon and a screen-film based imaging system for thoracic radiography," *Med. Phys.* **26**(7), 1349–1358 (1999).

<sup>9</sup>S. Peer, U. Neitzel, S. M. Giacomuzzi, R. Peer, E. Gassner, I. Steingruber, and W. Jaschke, "Comparison of low-contrast detail perception on storage phosphor radiographs and digital flat panel detector images," *IEEE Trans. Med. Imaging* **20**(3), 239–242 (2001).

<sup>10</sup>J. A. Segui and W. Zhao, "Performance of direct and indirect detection methods for digital mammography," 7th International Workshop on Digital Mammography (2004).

<sup>11</sup>N. W. Marshall, K. Faulkner, H. P. Busch, and K. J. Lehmann, "The contrast-detail behaviour of a photostimulable phosphor based computer radiography system," *Phys. Med. Biol.* **39**, 2289–2303 (1994).

<sup>12</sup>A. E. Burgess, F. L. Jacobson, and P. F. Judy, "Human observer detection experiments with mammograms and power-law noise," *Med. Phys.* **28**(4), 419–437 (2001).

<sup>13</sup>B. Grosjean and S. Muller, "Impact of textured background on scoring of simulated CDMAM phantom," *Lect. Notes Comput. Sci.* **4046**, 460–467 (2006).

<sup>14</sup>F. O. Bochud, J. F. Valley, F. R. Verdun, C. Hessler, and P. Schnyder, "Estimation of the noisy component of anatomical backgrounds," *Med. Phys.* **26**(7), 1365–1370 (1999).

<sup>15</sup>G. Borasi, A. Nitrosi, P. Ferrari, and D. Tassoni, "On site evaluation of three flat panel detectors for digital radiography," *Med. Phys.* **30**(7), 1719–1731 (2003).

<sup>16</sup>U. Neitzel, S. Gunther-Kohfahl, G. Borasi, and E. Samei, "Determination of the detective quantum efficiency of a digital X-ray detector: Comparison of three evaluations using a common image data set," *Med. Phys.* **31**(8), 2205–2211 (2004).

<sup>17</sup>A. Albanese, A. Bevilacqua, R. Campanini, E. Iampieri, N. Lanconelli, M. Rossi, D. Romani, V. Salomoni, and P. Vignoli, "Characterization of an FFDM unit based on a-Se direct conversion detector," *Digital Mammography: IWDM2002, 6th International Workshop on Digital Mammography* (Springer, New York, 2000), pp. 69–71.

<sup>18</sup>S. Rivetti, L. Angelini, M. Bertolini, R. Campanini, B. Canossi, C. Danielli, N. Lanconelli, S. Maggi, A. Nitrosi, and G. Borasi, "Physical characterization and contrast-detail analysis of different mammography units," 7th International Workshop on Digital Mammography (2004).

<sup>19</sup>International Electrotechnical Commission, "Medical diagnostic X-ray equipment—Radiation conditions for use in the determination of characteristics," (IEC-61267, Geneva, Switzerland, 2003).

<sup>20</sup>A. Burgess, "On the noise variance of a digital mammography system," *Med. Phys.* **31**(7), 1987–1995 (2004).

<sup>21</sup>J. T. Dobbins, D. L. Ergun, L. Rutz, D. A. Hinshaw, H. Blume, and D. C. Clark, "DQE(f) of four generations of computed radiography acquisition devices," *Med. Phys.* **22**, 1581–1593 (1995).

<sup>22</sup>J. M. Boone, "Spectral modeling and compilation of quantum fluence in radiography and mammography," *Proc. SPIE* **3336**, 592–601 (1998).

<sup>23</sup>J. M. Boone, T. R. Fewell, and R. J. Jennings, "Molybdenum, rhodium, and tungsten anode spectral models using interpolating polynomials with application to mammography," *Med. Phys.* **24**(12), 1863–1874 (1997).

<sup>24</sup>M. L. Giger and K. Doi, "Investigation of basic imaging properties in digital radiography. 3. Effect of pixel size on SNR and threshold contrast," *Med. Phys.* **12**(2), 201–208 (1985).

<sup>25</sup>G. Borasi, E. Samei, M. Bartolini, A. Nitrosi, and D. Tassoni, "Contrast-detail analysis of three flat panel detectors for digital radiography," *Med. Phys.* **33**(6), 1707–1719 (2006).

<sup>26</sup>J. A. Thomas, K. Chakrabarti, R. Kaczmarek, and A. Romanyukha, "Contrast-detail phantom scoring methodology," *Med. Phys.* **32**(3), 807–814 (2005).

<sup>27</sup>N. W. Marshall, "A comparison between objective, and subjective image quality measurements for a full-field digital mammography system," *Phys. Med. Biol.* **51**, 2441–2463 (2006).

<sup>28</sup>K. E. Applegate, R. Tello, and J. Ying, "Hypothesis testing III: Counts and medians," *Radiology* **228**(3), 603–608 (2003).

- <sup>29</sup>B. Lazzari, G. Belli, C. Gori, and K. Nykanen, Proc. SPIE **5030**, 656–666 (2003).
- <sup>30</sup>V. Loustauneau, M. Bisonnette, S. Cadieux, M. Hansrou, E. Masson, S. Savard, B. Polischuk, and M. Lehtimaki, “Imaging performance of a clinical selenium flat-panel detector for advanced applications in full-field digital mammography,” Proc. SPIE **5030**, 1010–1020 (2003).
- <sup>31</sup>B. Zhao and W. Zhao, “Characterization of a direct, full-field flat-panel digital mammography detector,” Proc. SPIE **5030**, 157–167 (2003).
- <sup>32</sup>S. Suryanarayanan, A. Karellas, and S. Vedantham, “Physical characteristics of a full-field digital mammography system,” Nucl. Instrum. Methods Phys. Res. A **533**, 560–570 (2004).
- <sup>33</sup>A. K. Carton, H. Bosmans, C. Vanongeval, G. Souverijns, G. Marchal, J. Jacobs, D. Vandembroucke, H. Pauwels, and K. Nijs, “Contrast threshold of 4 full field digital mammography systems using different measurements methods,” Lect. Notes Comput. Sci. **4046**, 593–600 (2006).
- <sup>34</sup>J. P. Moy, “Signal-to-noise ratio and spatial resolution in x-ray electronic imagers: is the MTF a relevant parameter?” Med. Phys. **27**(1), 86–93 (2000).